Electronic supplementary materials

For https://doi.org/10.1631/jzus.A2500352

Aerodynamic optimization of an externally tilted hex-rotor hovering unmanned aerial vehicle

Hengxing YANG[1], Yao LEI[1,2], Jifu HU[1], Guobin SHI[3]

[1]*School of Mechanical Engineering and Automation, Fuzhou University, Fuzhou 350116, China*
[2]*Key Laboratory of Fluid Power and Intelligent Electro-Hydraulic Control (Fuzhou University), Fujian Province University, Fuzhou 350116, China*
[3]*School of Intelligent Systems Engineering, Sun Yat-sen University, Shenzhen 518000, China*

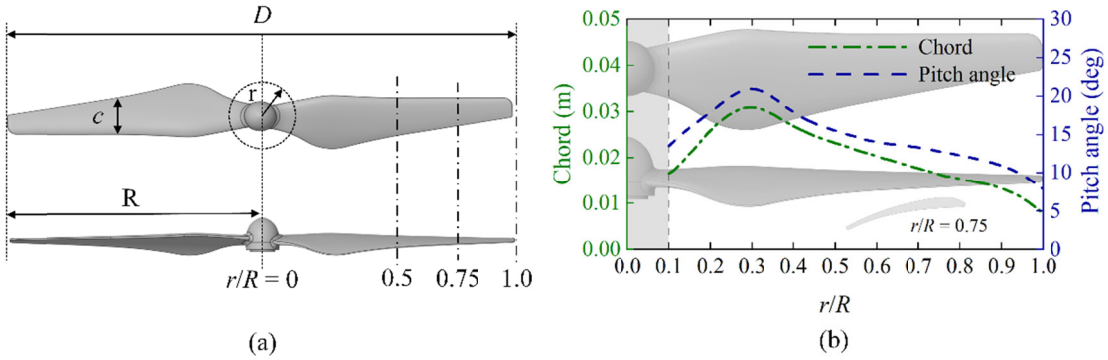

Fig. S1 Geometric model of the rotor: (a) top and front view; (b) rotor profile

Table S1 Key specifications of sensors

Facility	Model	Measured quantity	Scope	Accuracy (F.S.)
Thrust sensor	DYZ-101	Thrust	0–10 N	0.03%
Torque sensor	DYJN-104	Torque	0–0.5 N·m	0.05%
Hall sensor	NJK-8001C	RPM	10–9999 r/min	0.1%

Table S2 Specifications of the measured variables

Quantity	Source	Variable	Unit
Thrust	Thrust sensor	T	N
Torque	Torque sensor	M	N·m
Rotational speed	Hall sensor	Ω	r/min
Voltage	Power supply	V	V
Current	Current acquisition module	A	A
Atmospheric pressure	Weather services	P_{atm}	Pa
Air temperature	Thermograph	T_{air}	K

Eq. (S1) Rotor Characteristics

The rotor operation is characterized by a low Reynolds number, under the condition that the free stream speed is neglected (Garofano-Soldado et al., 2022; Jaroslawski et al., 2022):

$$Re_{75\%} = \frac{\rho V_{\omega} c_{75\%}}{\mu}. \tag{S1}$$

air density ρ = 1.223 kg/m³, linear velocity $V_{\omega} = \omega R_{75\%}$, dynamic viscosity μ = 1.7894 × 10^{-5} kg/(m·s), and angular velocity $\omega = \Omega\pi/30$ rad/s. Here, $R_{75\%}$ and $c_{75\%}$ denote the radius and chord length at the 75% spanwise position, respectively.

Section S1 Basis for selection of rotor spacing and tilt angle

Guided by prior experimental findings (Lei et al., 2018), which identified peak aerodynamic interference and performance degradation at a spacing of $L = 1.0D$, the spacing in this study was constrained to a range from $L = 1.2D$ to $L = 2.0D$. The lower limit prevents rotor collision, while the upper limit avoids overly large configurations that would degrade agility. Within this defined range, the spacing was varied in discrete increments of $0.2D$. This discretization allows the analysis to resolve how gradual changes in downwash overlap modulate the intensity of inter-rotor interference, ensuring sufficient parametric resolution to capture potential nonlinear flow effects.

For tilt angles, an 8°incremental step (8°, 16°, ..., 40°) was chosen to precisely track variations in thrust and torque. This step size balances analytical rigor, preventing data gaps that might obscure critical aerodynamic transitions, with experimental feasibility, yielding systematic datasets to map the boundary between beneficial flow synergy and detrimental turbulence. The selection of 8° increments was guided by preliminary CFD simulations conducted prior to the main parameter sweep, which indicated that significant aerodynamic transitions occur at angular intervals of approximately 10°–15°. An 8° step size ensures at least one intermediate data point between these critical transition zones, thereby capturing nonlinear variations in vortex coupling and downwash convergence without excessive computational cost.

Fundamentally, this represents a parameter sweep methodology based on discrete increments (spacing interval of $0.2D$ and tilt angle step of 8°), which constitutes an effective compromise between computational resource constraints and comprehensive exploration of the parameter space. The selected parameter range (i = 0.5–0.83, θ = 0°–40°) was determined based on prior experimental studies (Lei et al., 2018) and preliminary simulations, encompassing critical regimes from strong to weak aerodynamic interference and from zero to excessive tilt angles. This systematic approach ensures the identification of performance peaks and transitions in flow field mechanisms. Consequently, the configuration identified as optimal through this methodology is valid and representative for the specific system examined in this study.

Section S2 Description of the system

The dynamic behavior of an n-rotor system is characterized by the following matrix equation (Quintana et al., 2018):

$$\underbrace{\begin{bmatrix} m\boldsymbol{I}_3 & \boldsymbol{0}_3 \\ \boldsymbol{0}_3 & \boldsymbol{J} \end{bmatrix}}_{\boldsymbol{M}} \underbrace{\begin{bmatrix} \ddot{p} \\ \dot{\omega} \end{bmatrix}}_{\boldsymbol{a}} = \underbrace{\begin{bmatrix} -mg\hat{z} \\ -\omega \times \boldsymbol{J}\omega \end{bmatrix}}_{\boldsymbol{f}} + \underbrace{\begin{bmatrix} \boldsymbol{R}_r & \boldsymbol{0}_3 \\ \boldsymbol{0}_3 & \boldsymbol{I}_3 \end{bmatrix}}_{\boldsymbol{B}} \underbrace{\begin{bmatrix} \boldsymbol{F}_1 \\ \boldsymbol{F}_2 \end{bmatrix}}_{\boldsymbol{F}} \boldsymbol{u}. \tag{S2}$$

n denotes the number of rotors; m represents the multirotor mass; $\boldsymbol{0_3}$ represents a 3×3 zero matrix; $\boldsymbol{J}$ is the multirotor moment of inertia; $\boldsymbol{p}$ indicates the multirotor position with respect to the inertial frame; ω denotes the angular velocity about roll, pitch, and yaw with respect to the body frame; g is the gravitational acceleration; $\boldsymbol{R_r}$ is the rotation matrix mapping from the body frame to the inertial frame; $\hat{\boldsymbol{z}}$ is defined as $\hat{\boldsymbol{z}} = [0,0,1]^T$; and $\boldsymbol{u}$ serves as the control input vector.

In this study, the design of a hex-rotor (n = 6) is investigated. Matrix $\boldsymbol{F}$ serves as the allocation matrix for the total wrench exerted on the multirotor. Matrices $\boldsymbol{F_1}$ and $\boldsymbol{F_2}$ represent the force and moment matrices, respectively. Matrix $\boldsymbol{F_1} \in R^{3\times n}$ is composed of unit vectors $\boldsymbol{v_i} \in R^{3\times 1}$, which define the orientation of the i-th rotor. The magnitude of $\boldsymbol{v_i}$ is given by $\|\boldsymbol{v_i}\| = k_f$, where k_f is the coefficient that correlates the spinning velocity with the thrust. Matrix $\boldsymbol{F_2} \in R^{3\times n}$ consists of vectors $\boldsymbol{w_i} \in R^{3\times 1}$, which represent the combined torque resulting from thrust and drag moment.

$$w_i = k_m \sigma_i v_i + r_i \times v_i. \tag{S3}$$

Forces in the three coordinate directions are calculated based on the orientation of each rotor. The unit vector $\boldsymbol{v_i}$ decomposes into components along the x, y, and z axes, where its magnitude is given by $\|\boldsymbol{v_i}\| = k_f$. For a rotor tilted at angle θ, the x component of $\boldsymbol{v_i}$ is proportional to sin θ, the y component depends on the rotor's angular position around the central axis, and the z component is proportional to cos θ. Summing these components across all six rotors yields the total force in each coordinate direction.

Specifically, according to the Eq. (S3), where r_i is the position vector from the i-th rotor to the UAV's center of gravity. Here, k_m is a coefficient that relates the spinning velocity to the torque generated around the rotation axis, and σ_i indicates the direction of rotation, with $\sigma_i \in \{-1,1\}$. To counterbalance the torque (drag moment) of each rotor, the value of σ_i is defined as $\sigma_i = -1^i$.

Section S3 Error and uncertainty analysis

To ensure the accuracy of thrust measurements, thrust sensors were calibrated while mounted on the test stand. This approach mitigated any potential alterations in calibration factors due to structural preloading. The range of thrust values measurable by the balance is inherently defined by the maximum rating of the sensors. It is crucial to note, however, that the thrust cell experiences preloading from the stem and transmission structure, a factor that must be accounted for in the calibration process. Additionally, the rotational acceleration of the blades needs to be maintained within reasonable bounds, taking into consideration their mass.

The primary sources of error in the experiments stem from the standard deviations of the rotational speed and the mean voltages from the thrust sensors. The measurement error associated with the speed is influenced by the number of magnets in the motor. For a given measurement time t, the error for a single pulse with a speed variation is as follows:

$$n' = \frac{60\left(m_1 \pm 1\right)}{pt} = \frac{60m_1}{pt} \pm \frac{60}{pt}. \tag{S4}$$

where n' represents the rotational speed for the subsequent pulse; m_1 denotes the number of pulses; and p signifies the number of pulses produced per rotation.

The relative error ε is (Prothin et al., 2019; Leishman et al., 2008):

$$\varepsilon = \frac{\Delta n}{n} = \frac{1}{m_1}. \tag{S5}$$

$$m_1 = \frac{npt}{60}. \tag{S6}$$

$$\varepsilon = \frac{60}{pt} \times \frac{1}{n}. \tag{S7}$$

ε represents the relative error, n is the rotational speed (r/s), and Δn is the absolute error of the speed.

Given that the motor contains 24 magnets, $p = 24$, and the relative error is expressed as $\varepsilon = 60/(24tn)$. Typically, the standard deviation of thrust measurements is approximately 1% of the mean values. All uncertainty values presented in this study are calculated at a 95% confidence level.

From Eqs. (5) and (8), the PL is explicitly expressed in terms of the measured thrust T, torque Q, and angular velocity ω. it can be derived that:

$$\mathrm{PL} = \frac{T}{Q\omega}. \tag{S8}$$

According to Eq. (S8), the combined standard uncertainty of PL is evaluated by applying the first-order GUM (Guide to the Expression of Uncertainty in Measurement) propagation approach, assuming independent measurements:

$$u_{\mathrm{PL}}^2 = \left(\frac{\partial \mathrm{PL}}{\partial T}\right)^2 u_T^2 + \left(\frac{\partial \mathrm{PL}}{\partial Q}\right)^2 u_Q^2 + \left(\frac{\partial \mathrm{PL}}{\partial \omega}\right)^2 u_\omega^2. \tag{S9}$$

This leads to the following compact relationship:

$$\left(\frac{u_{\mathrm{PL}}}{\mathrm{PL}}\right)^2 = \left(\frac{u_T}{T}\right)^2 + \left(\frac{u_Q}{Q}\right)^2 + \left(\frac{u_\omega}{\omega}\right)^2. \tag{S10}$$

u_x^2 is the variance, and u_x is the standard uncertainty.

The angular speed is evaluated using the pulse counting relation given in Eq. (S7). Given the relation $\omega = \Omega\pi/30$, which represents a constant scaling, the relative uncertainty therefore remains invariant:

$$\frac{u_\omega}{\omega} = \frac{u_n}{n} = \frac{u_\Omega}{\Omega} = \varepsilon. \tag{S11}$$

The expanded uncertainty is given by $U_{\mathrm{PL}} = k u_{\mathrm{PL}}$. In line with the 95% confidence level specified above, a two-sided coverage factor of $k = 2$ is used, which is deemed appropriate for distributions with approximately normal errors and large effective degrees of freedom. To ensure a clear presentation of the measurement precision, all key measured values and their associated uncertainties are reported with 95% confidence intervals in Table S3.

Table S3 Key measured values with 95% confidence interval uncertainties

Value	Unit	Uncertainty
T	N	1.6%
P	W	1.5%
FM	-	2.8%
PL	-	2.2%
Ω	r/min	0.2%

Section S4 Mesh independence verification

To verify that the simulation results are independent of mesh resolution, a mesh independence study was conducted by employing various mesh sizes for the configuration with i = 0.56, θ = 24°. The mesh was progressively refined from mesh 1 (coarsest) to mesh 5 (finest), as illustrated in Fig. S2. Table S4 presents mesh independence studies for the configuration with i = 0.56. The 13.4 million-cell mesh yielded C_T and C_p relative errors <1.0% compared to 20 million-cell grids, confirming consistent accuracy across parameter ranges.

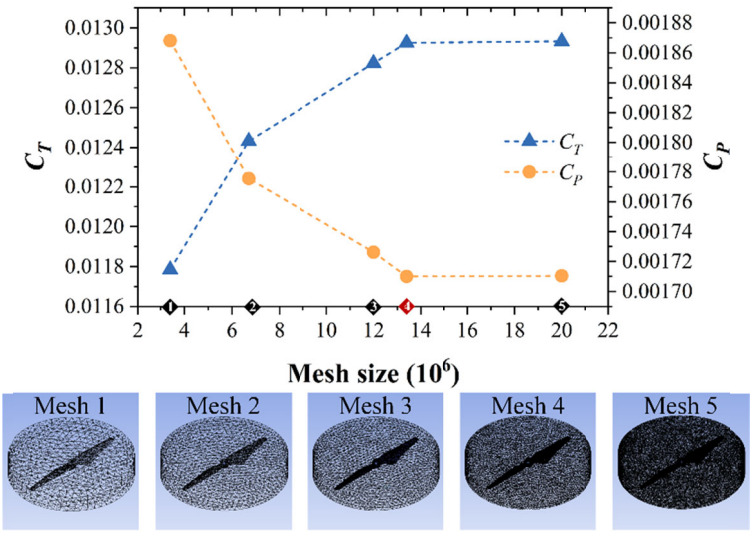

Fig. S2 Simulation results of thrust and power with different mesh sizes at i = 0.56, θ = 24°

Table S4 Mesh independence at i = 0.56, θ = 24°

Quantity	Source	Variable	Unit
Thrust	Thrust sensor	T	N
Torque	Torque sensor	M	N·m
Rotational speed	Hall sensor	Ω	r/min
Voltage	Power supply	V	V
Current	Current acquisition module	A	A
Atmospheric pressure	Weather services	P_{atm}	Pa
Air temperature	Thermograph	T_{air}	K

Moreover, since the flow field and the rotor system share the same fundamental characteristics, the mesh independence demonstrated for the specific configuration mentioned above is applicable to all other tested configurations. All configurations examined use rotors with the same diameter D = 240 mm and operate at the same rotational speed Ω = 5,500 r/min, which define the critical length and time scales of the flow. These scales remain consistent across the tested range of spacing ratios (i = 0.5–0.83) and tilt angles (θ = 0°–40°), as the variations in spacing and tilt do not introduce flow features that would require finer mesh resolution.

Section S5 Validation analysis

The relative error ε between the experimental and simulated values is defined as:

$$\varepsilon = \frac{X_{\text{sim}} - X_{\text{exp}}}{\left|X_{\text{exp}}\right|} \times 100\%. \tag{S12}$$

X_{sim} denotes the simulated value, and X_{exp} denotes the experimental value.

At each rotor spacing ratio i, a baseline is established using the planar configuration ($\theta = 0°$), with the corresponding performance metrics denoted as $T_0(v)$, $P_0(v)$, $\text{FM}_0(v)$ and $\text{PL}_0(v)$. These metrics are reported using both absolute and normalized values:

$$T^*(\theta, i) = \frac{T(\theta, i)}{T_0(i)}. \tag{S13}$$

$$P^*(\theta, v) = \frac{P(\theta, i)}{P_0(i)}. \tag{S14}$$

$$\text{FM}^*(\theta, i) = \frac{\text{FM}(\theta, i)}{\text{FM}_0(i)}. \tag{S15}$$

$$\text{PL}^*(\theta, i) = \frac{\text{PL}(\theta, i)}{\text{PL}_0(i)} = \frac{T(\theta, i) P_0(i)}{P(\theta, i) T_0(i)}. \tag{S16}$$

By eliminating the influence of run-to-run variations, this normalization isolates the specific effect of the tilt angle while maintaining the physical significance of Eq. (8) under matched i and θ conditions.

Numerical simulations were validated against experimental measurements, with Fig. S3 comparing thrust and power. Additionally, Table S5 presents selected normalized results from both experiments and simulations for various spacings and tilt angles. enabling broader generalization of the findings. The data show good agreement, with relative errors within 6%, confirming the model's ability to capture key aerodynamic trends.

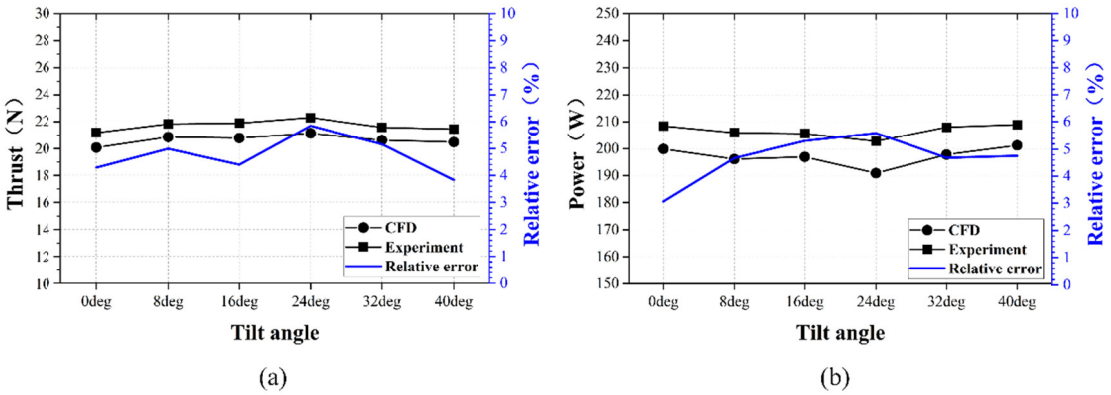

Fig. S3 relative error between the experimental results and the simulation results ($\bar{i}$ = 0.56): (a) thrust error; (b) power error

Table S5 Comparison of normalized experimental and CFD results

i	θ (°)	T^*_{exp}	P^*_{exp}	FM^*_{exp}	PL^*_{exp}	T^*_{CFD}	P^*_{CFD}	FM^*_{CFD}	PL^*_{CFD}
0.71	8	1.025	0.991	1.047	0.997	1.002	0.996	1.007	0.998
0.71	24	1.033	0.977	1.075	1.003	1.026	0.981	1.059	1.007
0.71	40	1.016	1.002	1.022	1.035	1.004	1.012	1.015	0.994
0.63	8	1.022	1.001	1.033	0.999	1.007	0.995	1.015	1.002
0.63	24	1.041	0.981	1.084	1.007	1.034	0.977	1.077	1.011
0.63	40	1.020	1.008	1.021	1.009	1.012	1.008	1.010	1.020
0.56	8	1.031	0.988	1.059	1.032	1.020	0.991	1.039	1.011
0.56	24	1.053	0.973	1.111	1.038	1.044	0.969	1.011	1.100
0.56	40	1.013	1.002	1.017	0.995	1.004	1.002	1.005	1.004

Section S6 Simulation analysis of rotor surface velocity and pressure distribution

Fig. S4 presents the surface velocity and pressure distributions on the rotor blades. The rotor tip velocity V_{tip} is defined as the linear speed at the rotor blade tip, calculated from the rotational speed Ω and rotor radius R. Data are extracted at the outermost point of each rotor blade, corresponding to the maximum radial distance from the center. As shown in Fig. S4, slight variations in V_{tip} occur even among symmetrically mounted rotors, originating from subtle differences in the local flow fields. Despite the symmetric geometry, adjacent rotors are subjected to varying levels of vortex interference due to their alternating rotation directions (P-N-P-N-P-N). At larger tilt angles (32° and 40°), this interference intensifies: cross-stream disturbances and asymmetric recirculation zones disrupt the inflow uniformity, leading to more pronounced discrepancies in V_{tip} across different rotors. Conversely, at tilt angle of 24°, stabilized primary vortex structures and constrained recirculation zones minimize such interference, resulting in closely clustered V_{tip} values (73.25 m/s–73.68 m/s), as observed.

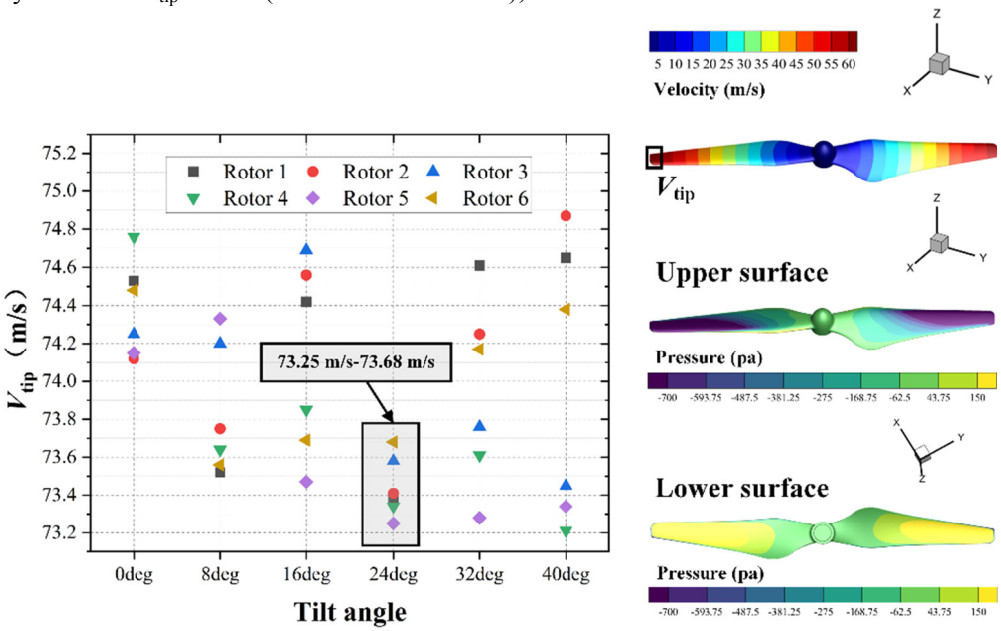

Fig. S4 Rotor characteristic with different configurations at i = 0.56: (a) rotor tip velocity; (a) pressure distributions over rotor surfaces at i = 0.56, θ = 24°

Fig. S4 provides a detailed view of the flow characteristics at θ = 24°, where a distinct pressure differential is evident: a high-pressure zone (yellow) on the lower surface and a low-pressure zone (purple) on the upper surface. This differential, essential for lift generation,

corresponds to the observations in Fig. 11. Furthermore, the surface velocity distribution transitions smoothly without abrupt gradients, indicating robust boundary layer attachment and no significant flow separation. This attached flow sustains high aerodynamic efficiency.

References

Garofano-Soldado A, Sanchez-Cuevas PJ, Heredia G, et al., 2022. Numerical-experimental evaluation and modelling of aerodynamic ground effect for small-scale tilted propellers at low Reynolds numbers. *Aerosp. Sci. Technol.*, 126(2):107625. https://doi.org/10.1016/j.ast.2022.107625

Jaroslawski T, Forte M, Moschetta JM, et al., 2022. Characterisation of boundary layer transition over a low Reynolds number rotor. *Exp. Therm. Fluid Sci.*, 130(2):110485. https://doi.org/10.1016/j.expthermflusci.2021.110485

Lei Y, Ji Y, Wang C, 2018. Optimization of aerodynamic performance for co-axial rotors with different rotor spacings. *Int. J. Micro Air Veh.*, 10(4):373-382. https://doi.org/10.1177/1756829318804763

Leishman JG, Syal M, 2008. Figure of merit definition for coaxial rotors. *J. Am. Helicopter Soc.*, 53(3):290-300. https://doi.org/10.4050/JAHS.53.290

Prothin S, Fernandez Escudero C, Doué N, et al., 2019. Aerodynamics of MAV rotors in ground and corner effect. *Int. J. Micro Air Veh.*, 11:175682931986159. https://doi.org/10.1177/1756829319861596

Quintana VA, Flores EAP, Merchan E, 2018. Multi-Objective Design Optimization of a Hexa-Rotor With Disturbance Rejection Capability Using an Evolutionary Algorithm. *IEEE Access*, 6:69064-69074. https://doi.org/10.1109/ACCESS.2018.2878314